

Porous boron nitride for combined CO₂ capture and photoreduction

Ravi Shankar,^{a,b} Anna Hankin^b and Camille Petit^{a,b,}*

^aBarrer Centre, Imperial College London, South Kensington Campus, Exhibition Road, London SW7 2AZ, United Kingdom

^bDepartment of Chemical Engineering, Imperial College London, South Kensington Campus, Exhibition Road, London SW7 2AZ, United Kingdom

*Corresponding author:

E-mail: camille.petit@imperial.ac.uk; Phone: +44 (0)20 7594 3182 (C. Petit)

Abstract

Porous and amorphous materials are typically not employed for photocatalytic purposes as their high number of defects can lead to low charge mobility and favour bulk electron-hole recombination. Yet, with a disordered nature can come porosity, which in turns promotes catalyst/reactant interactions and fast charge transfer to reactants. Here, we demonstrate that moving from *h*-BN, a well-known crystalline insulator to amorphous BN, we create a semiconductor, which is able to photoreduce CO₂ in a gas/solid phase, under both UV-vis and pure visible light, ambient conditions, without the need for cocatalysts. The material selectively produces CO and maintains its photocatalytic stability over several catalytic cycles. The performance of this un-optimised material is on par with that of TiO₂, the benchmark in the field. Owing to the chemical and structural tuneability of porous BN, these findings highlights the potential of porous BN-based structure for photocatalysis and particularly solar fuels production.

Keywords: boron nitride, photocatalysis, CO₂ photoreduction, solar fuel, porous materials.

With a push towards sustainable energy technologies, the share of renewables is projected to significantly increase in the years and decades to come.¹ Solar fuel production *via* photocatalysis represents one such energy generation route, allowing to directly take advantage of sunlight. Solar fuels include H₂ and O₂ derived from water splitting and carbon-based molecules (*e.g.* CH₄, CO, CH₃OH, etc...) derived from CO₂ reduction. Literature on CO₂ photoreduction catalysts is comparatively less extensive than on H₂ and O₂ generation, owing to the significant thermodynamic and kinetics limitations of this particular reaction. In fact, about 40 years after the work of Inoue *et al.* (1979), TiO₂ remains the benchmark in the field.² Researchers have looked at expanding the range of viable photocatalysts with works reported on derivatives of TiO₂, metal oxides, oxynitrides, carbon nitride, metal-organic frameworks and composites thereof.³⁻¹⁶ Overall, these studies concentrate on optimizing light absorption, preventing charge recombination, enhancing material robustness and controlling surface-catalysed reaction mechanisms and selectivity. For the most part, they focus on metal-based crystalline materials with low porosity. The latter feature limits the development of gas phase CO₂ photoreduction, which would allow integrated CO₂ capture and conversion set-ups. In addition, the usage of a rare metals either as part of the photocatalyst or as co-catalysts can be a barrier to large-scale deployment.

Here, taking into account the advent of graphitic carbon nitride, carbonaceous materials and other non-metal photocatalysts, we turn our attention to porous boron nitride (BN).¹⁷⁻²⁶ Porous BN exhibits key features of an ideal photocatalyst, yet it has never been studied for CO₂ photoreduction. The compelling features of BN include its metal-free nature as well as its tunable chemistry and structure that *a priori* allow for a tailored band structure.²⁷⁻²⁹ Porous BN is the amorphous analogue of hexagonal boron nitride (h-BN), a wide band gap insulator (~5.5 eV).³⁰ Doping of this robust material and its utilisation in composites have been employed to reduce the band gap and allow the formation of heterojunctions, respectively.³¹⁻³⁴ Today, the only reports of BN-based materials for CO₂ photoreduction are on carbon-doped BN³⁵⁻³⁸, which have since been shown to be unstable in the presence of moisture.^{39, 40}

Herein, we report a porous BN material as CO₂ adsorbent and CO₂ photoreduction catalyst under both UV and visible light. We explain how the structure and chemistry of the material control its adsorptive, optoelectronic and catalytic properties. This work paves the way for the creation of a new CO₂ photocatalyst platform.

Results and discussion

Porous BN – an adsorbent with semiconductor behaviour

The synthesis of this material was based on the previous work of Marchesini *et al.* (2017) and relied on a bottom-up pyrolytic synthesis at elevated temperatures using a mixture of boric acid, melamine and urea.⁴¹ To gain insight into the morphology and structure of the material, we collected high resolution transmission electron microscopy (HRTEM) images as well as X-ray diffraction (XRD) patterns (Figures 1a-c). Both techniques confirm the low degree of crystallinity of porous BN as opposed to *h*-BN. As seen on the HRTEM images, the range of stacked 2D layers is limited in porous BN (Figure 1a). In fact, the XRD patterns confirm the turbostratic nature of the material with only broad peaks at 2θ values of 26° and 44° , corresponding to the (002) and (100) planes, respectively. This contrasts with the sharp peaks for *h*-BN that indicates long range 3D/graphitic order. The d-spacing calculated from the TEM images and XRD peak (002) for *h*-BN and porous BN is 3.4 Å and 3.5 Å, respectively.^{42, 43 44} The d-spacing in porous BN is only relevant to the pseudo-crystalline regions of the material and is similar to that of *h*-BN. To characterize the structural features of the material at the micro/nano-scale, the specific surface area and porosity were analysed through nitrogen sorption at -196°C (Figure 1d for isotherms, Table S1 for textural parameters). Porous BN displays a BET equivalent specific surface area of $1585\text{ m}^2\text{ g}^{-1}$ and total pore volume of $1.10\text{ cm}^3\text{ g}^{-1}$, which is considerably larger than those for *h*-BN ($3\text{ m}^2\text{ g}^{-1}$ and nil porosity). The type I/IV isotherm with a type H3/H4 hysteresis loop observed for porous BN indicates the presence of slit-shaped micro- and mesopores. The high surface area of porous BN is key for interfacial phenomena, enhancing access to active CO_2 absorption and reduction sites. This is particularly important in gas phase schemes like the one proposed here, where CO_2 reduction is limited by the ability of the molecules to be adsorbed on the catalyst, close to the catalytic sites.

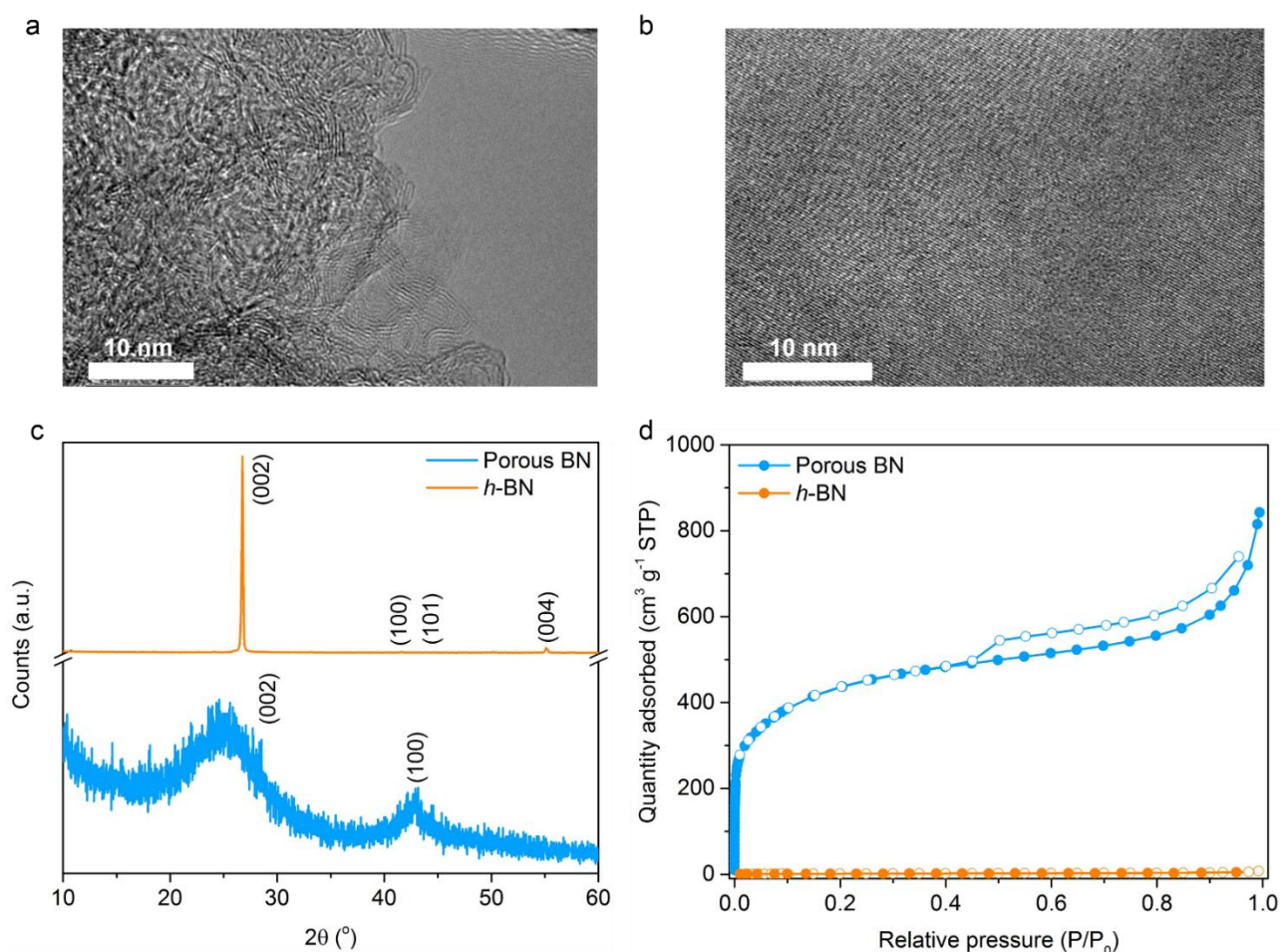


Figure 1 Structure and morphology of the porous BN sample compared to *h*-BN. (a) HRTEM image of the as-synthesized porous BN sample highlighting the porous morphology through the absence of stacked layers or wide crystalline domains, (b) HRTEM image of *h*-BN, taken for comparison, illustrating the high degree of crystallinity with a large number of stacked, well-ordered 2D layers, (c) Powder XRD patterns of porous BN and *h*-BN, (d) N₂ sorption isotherms for porous BN and *h*-BN measured at -196 °C.

We characterised the chemical structure and bonding types of the porous BN through Fourier transform infrared spectroscopy (FT-IR), energy dispersive X-ray spectroscopy (EDX) and X-ray photoelectron spectroscopy (XPS) (Figure 2). Again, we used *h*-BN here as a reference material. We observe the two characteristic IR bands of BN at $\sim 1380\text{ cm}^{-1}$ (in-plane B-N transverse stretching) and $\sim 800\text{ cm}^{-1}$ (out-of-plane B-N-B bending) in both samples,⁴⁵ while no B-O bands are noted (Figure 2a). Yet, elemental mapping conducted using SEM EDX points to the presence of oxygen homogeneously distributed through the structure (Figure 2b). To gain further insight into the relative atomic surface composition and chemical states of the

elements, we collected high resolution core level spectra through XPS (Supplementary Figure S1). The formation of BN in porous BN sample is confirmed through the fitted core level spectra of the B 1s and N 1s, showing the presence of B-N bonds (191.0 eV for B 1s and 398.5 eV for N 1s, Supplementary Figure S1).^{46, 47} In addition, we observe shake-up satellite peaks for B 1s and N 1s core level spectra for porous BN (Supplementary Figure S1), which provides evidence for the formation of a sp²-hybridised hexagonal BN phase.⁴⁸⁻⁵⁰ Further, XPS points to a significant proportion of oxygen in porous BN with a peak at 533.1 eV (10 at%, Figure 2c, Supplementary Figure S1). We attribute this peak to the borooxynitride (B-O_x-N_y) species, which stems from the in-plane substitution of oxygen atoms into the BN lattice, as we have described in a prior study.^{29, 51} Quite surprisingly, oxygen atoms are also observed on *h*-BN (6 at%) and are most likely related to edge hydroxyl groups. Oxygen atoms can enhance CO₂ adsorption^{52, 53} and can also allow lead to reduction in band gap, as indicated by both computational and experimental work.^{28, 54, 55} Both aspects are important in the context of CO₂ capture and photoconversion. The carbon contents in the samples are comparatively much lower (~ 3 at. % ± 1 at. %) and are linked to the presence of adventitious carbon impurities, *i.e.* not part of the material.

Next, we probed the optoelectronic properties of porous BN through UV-vis diffuse reflectance spectroscopy and chronoamperometry (Figure 2d-f). The light absorption spectrum (Figure 2d) of the material clearly indicates a red-shift when moving from *h*-BN to porous BN, with the absorption edge moving from 215 nm to around 300 nm. From the Tauc plot of the transformed Kubelka-Munk function against photon energy (Supplementary Figure S2), the porous BN sample exhibits a UV-range band gap of 4.21 eV, significantly lower than that of *h*-BN (~5.50 eV) (Figure 2e). These results point to the creation of a semiconducting porous BN material. At this stage, we cannot infer whether the semiconducting property is related to the presence of functional groups, their specific location on the BN nanosheets or the introduction of porosity. Cyclic voltammetry measurements showed that porous BN exhibits reproducible current responses across a wide applied potential range and an anodic current response, albeit small in magnitude, is observed (Figure S5). Through chrono amperometry (Figure 2f), the sample was irradiated with UV light, which was periodically switched on and off for multiple cycles. Porous BN electrode is able to generate and maintain a virtually constant photocurrent density (Figure 2f), which suggests that the material is indeed functioning as a photocatalyst by inducing electron-hole pairs. Considering the semiconducting nature of porous BN in

conjunction with its high surface area and porosity, we went on to test the material for combined CO₂ capture and photocatalytic reduction.

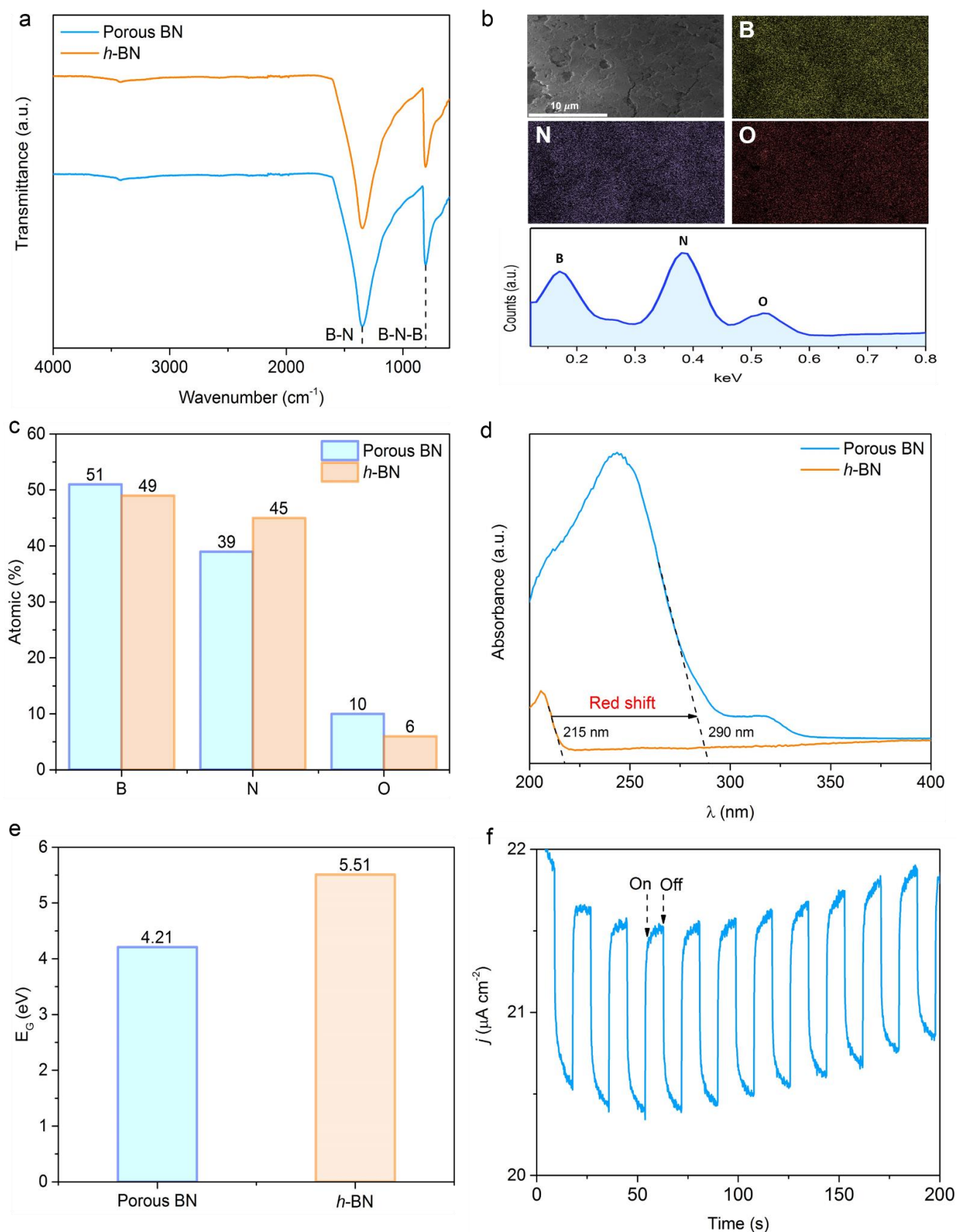


Figure 2. Chemical and optoelectronic properties of the porous BN sample compared to *h*-BN. (a) FT-IR spectra of as-synthesized porous BN, with key characteristic bands highlighted, and *h*-BN as a reference,

(b) SEM image, EDX spectrum and elemental mapping for porous BN showing the homogeneous distribution of the elements throughout the structure, (c) Relative atomic composition of porous BN obtained through XPS analysis, (d) Light absorption spectrum of the porous BN sample compared to that of *h*-BN, (e) Comparison of the band gap of porous BN, as obtained through UV-vis diffuse reflectance spectroscopy, with that of *h*-BN showing the semiconducting behaviour of porous BN, (f) Photocurrent generation from porous BN under UV-vis irradiation for multiple on/off cycles measured through current amperometry.

CO₂ photoreduction using porous BN

Prior to photocatalytic testing, the CO₂ adsorption capacity of the material at the reaction conditions was measured (25 °C, 0-1 bara) and compared to ‘reference’ materials, *i.e.* TiO₂ (benchmark in the field), *h*-BN (‘parent’ material of porous BN) and carbon nitride (g-C₃N₄, most closely related polymeric photocatalyst). Unsurprisingly, porous BN adsorbs significantly more CO₂ than the reference materials (Figure 3a), most likely due to its higher porosity (Table S1, textural parameters for all materials). We note in fact that several authors have already reported the use of porous BN as an adsorbent for CO₂ with similar capacities reported^{41, 52, 56, 57}. Next, we tested porous BN and the reference materials for the gas phase photoreduction of CO₂ under UV-vis and pure visible irradiation, without doping or the presence of a co-catalyst. The photocatalytic performance of the material was assessed using a CO evolution assay after an irradiation time of 5 hours. Under these conditions, the porous BN catalyst drove the photoreduction of CO₂ with an average specific CO production rate of 1.16 μmol g⁻¹ h⁻¹ (Figure 3b). The CO₂ photoreduction test was also conducted, under the same conditions, for P25, g-C₃N₄ and *h*-BN to compare the photocatalytic performance of porous BN. The CO₂ adsorption capacities at 25 °C and specific CO evolution rates of all of the materials investigated in this study are tabulated in Table S2. Under UV-vis irradiation, porous BN exhibits a higher specific CO production rate than those for the reference materials. We attribute the significant increase in CO production going from *h*-BN to porous BN to the increase in surface area and porosity as well as the greater light harvesting property. Porous BN is surpassed by g-C₃N₄ and P25 using visible irradiation, which is to be expected given the lower band gaps of these materials (2.72 eV and 3.20 eV, respectively). Such low band gap may be attainable in BN after significant O doping as suggested in the literature^{28, 54, 55}.

We confirmed the origin of CO through a number of control tests: absence of catalyst, dark mode and N₂/H₂ atmosphere (Table S3). All supported the fact that the source of the CO evolved stems from the photocatalytic reduction of CO₂. To further substantiate this claim, we carried out isotopic experiments using ¹³CO₂. Aside from ¹³CO₂ being used as the feed gas in tandem with H₂ as the sacrificial agent, the same catalyst preparation method and reaction conditions from the original system were maintained. The gas chromatogram corresponding to the ¹³CO peak and the mass spectra for the photocatalytic ¹³CO₂ reduction system are presented in Figure S4. The results point to the formation of ¹³CO and provides direct evidence that the origin of the evolved CO.

The kinetic study (Figure 3c) indicates a constant CO evolution rate over a 6-hour testing period, which shows that the catalyst is able to maintain its photoactivity throughout the course of the reaction. We tested further the recyclability of the catalyst over 3 cycles under UV vis irradiation (Figure 3d). We observed a 14% decrease in CO production after the third cycle (Figure 3d). Further, we checked the stability of the material through XRD pattern and observed a slight increase in crystallinity after CO₂ photoreduction (Figure S3). This finding suggests that amorphous domains of the material degraded upon reaction. This is supported by N₂ sorption tests, which showed a 25% decrease in porosity after reaction. Notably though, the porous BN sample still maintained a high surface area and porosity of 1196 m² g⁻¹ and 1.01 cm³ g⁻¹ (Supplementary Table S1).

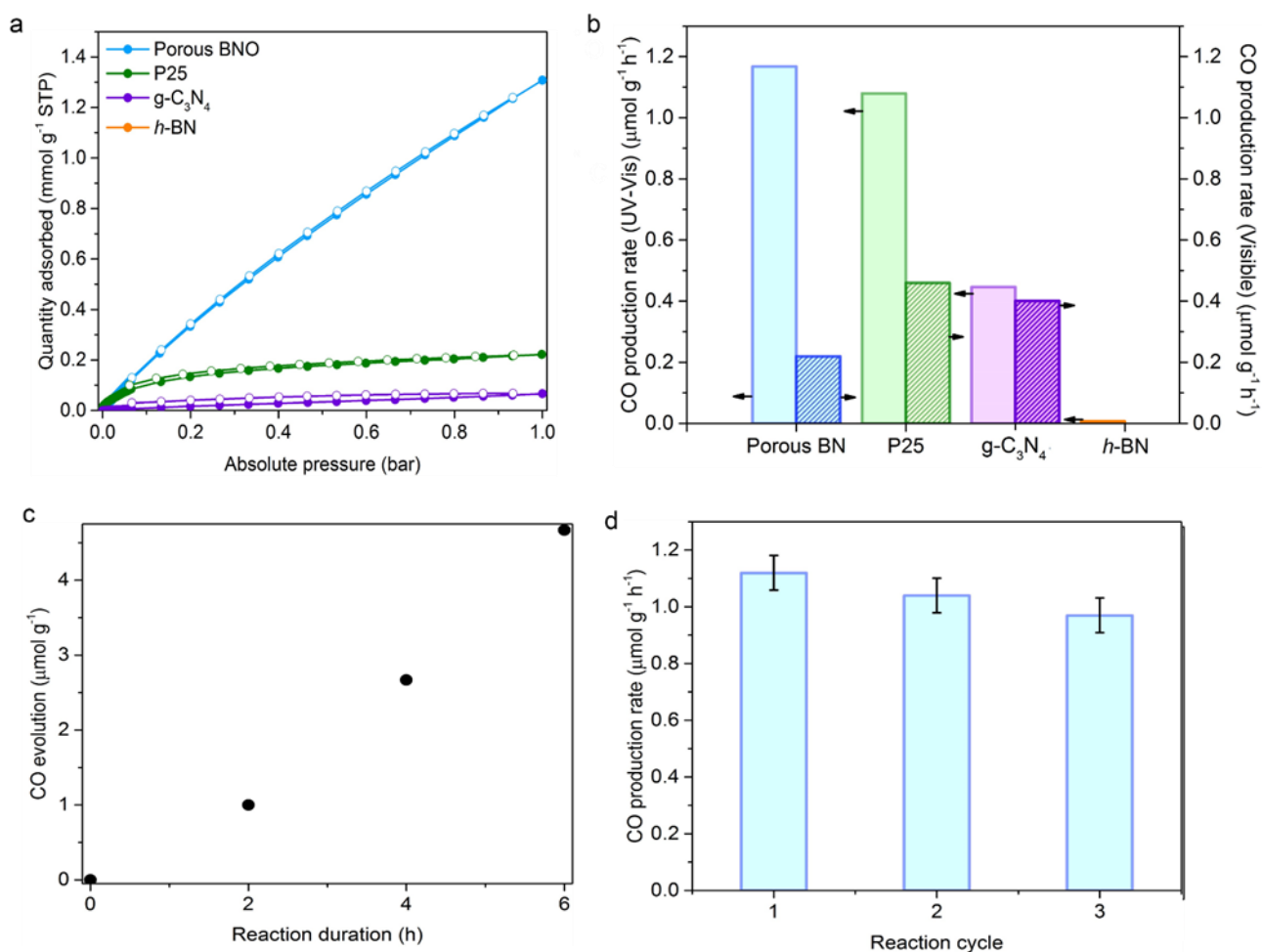


Figure 3. Photocatalytic testing of the porous BN sample. (a) CO₂ adsorption isotherms collected at 25 °C for the materials investigated in this study, (b) Specific production rate of CO for porous BN, compared to TiO₂ P25, h-BN and carbon nitride (g-C₃N₄) as reference materials, under UV-vis and pure visible light irradiation (300 W, Xe lamp, 5 hours, 25 °C), (c) Photocatalytic CO evolution from porous BN as a function of time, (d) CO evolution from porous BN repeated over three 5 hour photocatalytic cycles.

In summary, we introduce a new material platform based on porous BN material that is able to facilitate combined CO₂ capture and photoreduction in a simple gas/solid phase set-up under ambient conditions, without the use of co-catalysts. This material has never been reported for CO₂ photoreduction before. Unlike its crystalline counterpart, porous BN exhibits semiconducting behaviour and is able to photoreduce CO₂ to CO under both UV-vis and visible irradiations, at rates similar to higher than the benchmark in the field, *i.e.* P25 TiO₂. Porous BN exhibits a steady CO evolution rate over a single cycle and maintained about 85% of its

initial performance over multiple catalytic reactions. Given the chemical and structural tunability of this material, there is considerable scope to expand the photocatalyst functionality to the visible-light region and increase its rate performance. This would constitute a considerable stride in the field of solar fuels synthesis.

Methods

Synthesis of porous BN. In a typical synthesis, boric acid (H_3BO_3 , ACS reagent, 99.0 %, Sigma-Aldrich), urea ($\text{CH}_4\text{N}_2\text{O}$, molecular biology grade, Sigma-Aldrich), and melamine ($\text{C}_3\text{H}_6\text{N}_6$, ACS reagent, 99.0 %, Sigma-Aldrich), with a 1:1 molar ratio of boric acid to melamine and 1:5 molar ratio of boric acid to urea were mechanically mixed together and finely ground for 5 minutes in an agate mortar to form a homogeneous powder. The finely ground powder was subsequently transferred to an alumina boat crucible, which was placed in a horizontal tubular furnace. The sample was initially degassed at ambient temperature for 3 hours under an inert nitrogen atmosphere (flow rate of $250 \text{ cm}^3 \text{ min}^{-1}$). Once the degas was complete, the nitrogen flow rate was decreased to $50 \text{ cm}^3 \text{ min}^{-1}$, and the sample was heated from ambient temperature to 1050°C with a ramp rate of $10^\circ\text{C min}^{-1}$. This steady-state temperature was maintained for 3.5 hours, after which the samples were allowed to naturally cool to room temperature, whilst maintaining the same nitrogen flow rate. Upon completion of the synthesis, a porous white powder was obtained. The reference materials, *h*-BN and P25 TiO_2 , were obtained from Saint Gobain (Tres BN, max. particle size 74 nm) and Sigma (P25, >99.5%, 21 nm primary particle size).

Synthesis of g- C_3N_4 . In a typical synthesis, 12 g of melamine ($\text{C}_3\text{H}_6\text{N}_6$, ACS reagent, 99.0 %, Sigma-Aldrich) were weighed and transferred to an alumina crucible, which was placed in a muffle furnace. The sample was heated from ambient temperature to 560°C with a ramp rate of 5°C min^{-1} . This steady-state temperature was maintained for 4 hours, after which the samples were allowed to naturally cool to room temperature. Upon completion of the synthesis, a yellow solid product was obtained, which was subsequently ground in an agate mortar to form a fine, homogeneous powder.

Characterization. For FT-IR analysis, the samples were first ground to a powder using an agate mortar. Subsequently, the spectra were obtained in the range of $500 - 4000 \text{ cm}^{-1}$ using a Perkin-Elmer Spectrum 100

FT-IR spectrometer equipped with an attenuated total reflectance (ATR) accessory. X-ray photoelectron spectroscopy (XPS) to determine the relative elemental composition of the samples, as well as the chemical states of the elements, was conducted using a Thermo Scientific K-Alpha⁺ X-ray Photoelectron Spectrometer equipped with a MXR3 Al K α monochromated X-ray source ($h\nu = 1486.6$ eV). The samples were initially ground and mounted onto an XPS sample holder using a small rectangular piece of conductive carbon tape. The X-ray gun power was set to 72 W (6 mA and 12 kV). Survey scans were acquired using 200 eV pass energy, 0.5 eV step size and 100 ms (50 ms x 2 scans) dwell times. All of the high resolution spectra (B 1s, N 1s, C 1s, and O 1s) were obtained using a 20 eV pass energy and 0.1 eV step size. The results were analysed using the Thermo Advantage data analysis program.

Powder X-ray diffraction (XRD) was performed using a PANalytical X'Pert Pro X-ray diffractometer in reflection-transmission mode with a spinning stage (2 revolutions/second). An anode voltage of 40 kV and emission current of 20 mA were chosen as the operating conditions using a monochromatic Cu-K α radiation source ($\lambda = 1.54178$ Å). The X'Celerator silicon strip detector was used in the diffractometer. Nitrogen and CO₂ sorption isotherms were measured using a porosity and surface area analyser (Micrometrics 3 Flex) at -196 °C and 25 °C, respectively. The samples were initially degassed overnight at 120 °C at approximately 0.2 mbar pressure. Subsequently, prior to the sorption isotherm measurement, the samples were degassed in-situ for 4 hours at 120 °C. The equivalent specific surface areas of the samples were determined using the Brunauer-Emmett-Teller (BET) method.⁵⁸ The total pore volume was ascertained from the volume of N₂ adsorbed at a relative pressure (P/P_0) of 0.97. The micropore volume was determined using the Dubnin-Radushkevich model. Transmission Electron Microscopy (TEM) images were collected on a JEOL 2100Plus with 200 kV acceleration voltage. The samples were previously dispersed in ethanol and deposited on a carbon holey grid. SEM-EDX analysis was performed on an Auriga Zeiss microscope at 5 keV for both imaging and EDX analysis. The powder samples were compressed on a carbon tape and coated with 10 nm of gold.

Photocatalytic reduction of CO₂. A gas/solid photoreactor setup was assembled to conduct the photocatalytic reduction of CO₂. The as-synthesised, finely ground porous BN photocatalysts were deposited on a circular metal disc with a fixed area of 9.6 cm². To do so, 30 mg of porous BN powder was added to 1.5 mL of ethanol and stirred rapidly to form a homogeneous suspension, which was drop casted onto the sample holder. Research grade (99.999%) CO₂ and H₂ (99.9995%, Peak Scientific PH200 hydrogen generator) were flowed

at controlled rates using mass flow controllers (Omega Engineering, 0–50 mL/min). Firstly, the photoreactor (35 cm³) was vacuumed and replenished with a gas mixture of CO₂ and H₂ (1.5 vol/vol ratio) ten times. The same gas mixture of CO₂ and H₂ was subsequently passed over the catalyst bed in the photoreactor for 15 residence times before it was sealed at 1.25 bara and irradiated for 5 hours. A xenon arc lamp (300 W, $\lambda > 325$ nm, LOT Quantum Design), equipped with a water filter was used as the irradiation source. A UV filter ($\lambda < 400$ nm) was used to conduct the tests under visible light irradiation. The evolved gases were detected by a gas chromatograph (GC, Agilent Technologies) with HayeSep and molecular sieve columns in series, and thermal conductivity (TCD) and flame ionisation (FID) detectors. During the recyclability tests to assess the photostability of the materials, the aforementioned process was repeated after each 5-hour irradiation cycle without opening the photoreactor. In addition, isotopic tracing experiments were performed with ¹³CO₂ (BOC, >98% atom ¹³CO₂ compared to ¹²CO₂, >99%).

References

1. Centi, G.; Quadrelli, E. A.; Perathoner, S. *Energy & Environmental Science* **2013**, 6, (6), 1711-1731.
2. Inoue, T.; Fujishima, A.; Konishi, S.; Honda, K. *Nature* **1979**, 277, 637-638.
3. Crake, A.; Christoforidis, K. C.; Kafizas, A.; Zafeiratos, S.; Petit, C. *Applied Catalysis B: Environmental* **2017**, 210, 131-140.
4. Woolerton, T. W.; Sheard, S.; Reisner, E.; Pierce, E.; Ragsdale, S. W.; Armstrong, F. A. *Journal of the American Chemical Society* **2010**, 132, (7), 2132-2133.
5. Woolerton, T. W.; Sheard, S.; Pierce, E.; Ragsdale, S. W.; Armstrong, F. A. *Energy & Environmental Science* **2011**, 4, (7), 2393-2399.
6. Nunez, J.; Víctor, A.; Jana, P.; Coronado, J. M.; Serrano, D. P. *Catalysis Today* **2013**, 209, 21-27.
7. Yoshitomi, F.; Sekizawa, K.; Maeda, K.; Ishitani, O. *ACS applied materials & interfaces* **2015**, 7, (23), 13092-13097.
8. Zhang, N.; Ouyang, S.; Kako, T.; Ye, J. *Chemical Communications* **2012**, 48, (9), 1269-1271.
9. Crake, A. *Materials Science and Technology* **2017**, 33, (15), 1737-1749.
10. Li, R.; Zhang, W.; Zhou, K. *Advanced Materials* **2018**, 1705512.

11. Wang, C.; Thompson, R. L.; Ohodnicki, P.; Baltrus, J.; Matranga, C. *Journal of Materials Chemistry* **2011**, 21, (35), 13452-13457.
12. Liao, F.; Zeng, Z.; Eley, C.; Lu, Q.; Hong, X.; Tsang, S. C. E. *Angewandte Chemie International Edition* **2012**, 51, (24), 5832-5836.
13. Zhou, S.; Liu, Y.; Li, J.; Wang, Y.; Jiang, G.; Zhao, Z.; Wang, D.; Duan, A.; Liu, J.; Wei, Y. *Applied Catalysis B: Environmental* **2014**, 158, 20-29.
14. Lin, J.; Pan, Z.; Wang, X. *ACS Sustainable Chemistry & Engineering* **2013**, 2, (3), 353-358.
15. Qin, J.; Wang, S.; Ren, H.; Hou, Y.; Wang, X. *Applied Catalysis B: Environmental* **2015**, 179, 1-8.
16. Ohno, T.; Murakami, N.; Koyanagi, T.; Yang, Y. *Journal of CO2 Utilization* **2014**, 6, 17-25.
17. Wang, X.; Maeda, K.; Thomas, A.; Takanabe, K.; Xin, G.; Carlsson, J. M.; Domen, K.; Antonietti, M. *Nature materials* **2009**, 8, (1), 76.
18. Niu, P.; Qiao, M.; Li, Y.; Huang, L.; Zhai, T. *Nano Energy* **2018**, 44, 73-81.
19. Liang, Q.; Li, Z.; Yu, X.; Huang, Z. H.; Kang, F.; Yang, Q. H. *Advanced Materials* **2015**, 27, (31), 4634-4639.
20. Martin, D. J.; Qiu, K.; Shevlin, S. A.; Handoko, A. D.; Chen, X.; Guo, Z.; Tang, J. *Angewandte Chemie International Edition* **2014**, 53, (35), 9240-9245.
21. Shen, M.; Zhang, L.; Shi, J. *Nanotechnology* **2018**, 29, (41), 412001.
22. Tu, W.; Xu, Y.; Wang, J.; Zhang, B.; Zhou, T.; Yin, S.; Wu, S.; Li, C.; Huang, Y.; Zhou, Y.; Zou, Z.; Robertson, J.; Kraft, M.; Xu, R. *Acs Sustain Chem Eng* **2017**, 5, (8), 7260-7268.
23. Sun, Z.; Fischer, J. M. T. A.; Li, Q.; Hu, J.; Tang, Q.; Wang, H.; Wu, Z.; Hankel, M.; Searles, D. J.; Wang, L. *Applied Catalysis B: Environmental* **2017**, 216, 146-155.
24. Liu, J.; Wen, S.; Hou, Y.; Zuo, F.; Beran, G. J.; Feng, P. *Angewandte Chemie* **2013**, 125, (11), 3323-3327.
25. Wang, M.; Li, M.; Xu, L.; Wang, L.; Ju, Z.; Li, G.; Qian, Y. *Catalysis Science & Technology* **2011**, 1, (7), 1159-1165.
26. Li, X.; Zhao, J.; Yang, J. *Scientific reports* **2013**, 3, 1858.
27. Pang, J.; Chao, Y.; Chang, H.; Li, H.; Xiong, J.; He, M.; Zhang, Q.; Li, H.; Zhu, W. *Journal of colloid and interface science* **2017**, 508, 121-128.

28. Weng, Q.; Kvashnin, D. G.; Wang, X.; Cretu, O.; Yang, Y.; Zhou, M.; Zhang, C.; Tang, D. M.; Sorokin, P. B.; Bando, Y. *Advanced materials* **2017**, 29, (28).
29. Marchesini, S.; Regoutz, A.; Payne, D.; Petit, C. *Micropor Mesopor Mat* **2017**, 243, 154-163.
30. Kim, J.; Han, J.; Seo, M.; Kang, S.; Kim, D.; Ihm, J. *Journal of Materials Chemistry A* **2013**, 1, (4), 1014-1017.
31. Lei, W.; Portehault, D.; Dimova, R.; Antonietti, M. *Journal of the American Chemical Society* **2011**, 133, (18), 7121-7127.
32. Ci, L.; Song, L.; Jin, C.; Jariwala, D.; Wu, D.; Li, Y.; Srivastava, A.; Wang, Z.; Storr, K.; Balicas, L. *Nature materials* **2010**, 9, (5), 430.
33. Lu, J.; Zhang, K.; Liu, X. F.; Zhang, H.; Sum, T. C.; Neto, A. H. C.; Loh, K. P. *Nature communications* **2013**, 4, 2681.
34. Yin, L.-W.; Bando, Y.; Golberg, D.; Gloter, A.; Li, M.-S.; Yuan, X.; Sekiguchi, T. *Journal of the American Chemical Society* **2005**, 127, (47), 16354-16355.
35. Huang, C.; Chen, C.; Zhang, M.; Lin, L.; Ye, X.; Lin, S.; Antonietti, M.; Wang, X. *Nat Commun* **2015**, 6, 7698.
36. Zhou, M.; Wang, S.; Yang, P.; Huang, C.; Wang, X. *ACS Catalysis* **2018**, 8, (6), 4928-4936.
37. Li, J.; Lei, N.; Hao, H.; Zhou, J. *Chemical Physics Letters* **2017**, 672, 99-104.
38. Sivaprakash, K.; Induja, M.; Priya, P. G. *Materials Research Bulletin* **2018**, 100, 313-321.
39. Florent, M.; Bandoz, T. J. *J Mater Chem A* **2018**, 6, (8), 3510-3521.
40. Alkoy, S.; Toy, C.; Gönül, T.; Tekin, A. *Journal of the European Ceramic Society* **1997**, 17, (12), 1415-1422.
41. Marchesini, S.; McGilvery, C. M.; Bailey, J.; Petit, C. *ACS nano* **2017**, 11, (10), 10003-10011.
42. Lin, Y.; Connell, J. W. *Nanoscale* **2012**, 4, (22), 6908-6939.
43. Jiang, X.-F.; Weng, Q.; Wang, X.-B.; Li, X.; Zhang, J.; Golberg, D.; Bando, Y. *Journal of Materials Science & Technology* **2015**, 31, (6), 589-598.
44. Kurakevych, O. O.; Solozhenko, V. L. *Acta Crystallographica Section C: Crystal Structure Communications* **2007**, 63, (9), i80-i82.
45. Geick, R.; Perry, C.; Rupprecht, G. *Physical Review* **1966**, 146, (2), 543.

46. Ciofani, G.; Genchi, G. G.; Liakos, I.; Athanassiou, A.; Dinucci, D.; Chiellini, F.; Mattoli, V. *Journal of colloid and interface science* **2012**, 374, (1), 308-314.
47. Cholet, V.; Vandenbulcke, L.; Rouan, J.; Baillif, P.; Erre, R. *Journal of materials science* **1994**, 29, (6), 1417-1435.
48. Riviere, J.; Pacaud, Y.; Cahoreau, M. *Thin Solid Films* **1993**, 227, (1), 44-53.
49. Park, K.; Lee, D.; Kim, K.; Moon, D. *Applied physics letters* **1997**, 70, (3), 315-317.
50. Nazarov, A. S.; Demin, V. N.; Grayfer, E. D.; Bulavchenko, A. I.; Arymbaeva, A. T.; Shin, H. J.; Choi, J. Y.; Fedorov, V. E. *Chemistry–An Asian Journal* **2012**, 7, (3), 554-560.
51. Gouin, X.; Grange, P.; Bois, L.; L'Haridon, P.; Laurent, Y. *Journal of alloys and compounds* **1995**, 224, (1), 22-28.
52. Chen, Y.; Wang, J.; Chen, Y.; Liu, D.; Huang, S.; Lei, W. *Nanoscale* **2018**.
53. Lei, W.; Zhang, H.; Wu, Y.; Zhang, B.; Liu, D.; Qin, S.; Liu, Z.; Liu, L.; Ma, Y.; Chen, Y. *Nano Energy* **2014**, 6, 219-224.
54. Silva, L. A.; Guerini, S. C.; Lemos, V. *IEEE transactions on nanotechnology* **2006**, 5, (5), 517-522.
55. Wu, J.; Zhang, W. *Solid State Communications* **2009**, 149, (11-12), 486-490.
56. Sun, Q.; Li, Z.; Searles, D. J.; Chen, Y.; Lu, G.; Du, A. *Journal of the American Chemical Society* **2013**, 135, (22), 8246-8253.
57. Chen, S.; Li, P.; Xu, S.; Pan, X.; Fu, Q.; Bao, X. *Journal of Materials Chemistry A* **2018**, 6, (4), 1832-1839.
58. Brunauer, S.; Emmett, P. H.; Teller, E. *Journal of the American chemical society* **1938**, 60, (2), 309-319.

Acknowledgements

The authors would like to thank S. Marchesini for her help in producing the TEM images and to A. Crake for his technical input in the photocatalytic testing and isotopic testing, The authors would also like to acknowledge the funding from EPSRC through the Doctoral Partnership fund (1855454), which made this

research possible. We also acknowledge support from the Department of Chemical Engineering at Imperial College London.

Declaration

The authors declare that there are no competing financial interests.

Supplementary Information

Table S1. Key textural parameters derived from N₂ sorption isotherms obtained at -196°C for the materials investigated in this study.

Sample	S _{BET} (m ² g ⁻¹)	V _{tot} (cm ³ g ⁻¹)	V _{micro} (cm ³ g ⁻¹)	V _{micro} / V _{tot} (%)
Porous BN <i>Before CO₂ reaction</i>	1585	1.10	0.66	60.0
Porous BN <i>After CO₂ reaction</i>	1196	1.01	0.44	43.6
<i>h</i>-BN	3	0.006	0.001	16.7
P25	48	0.112	0.016	14.3
g-C₃N₄	32	0.164	0.020	12.1

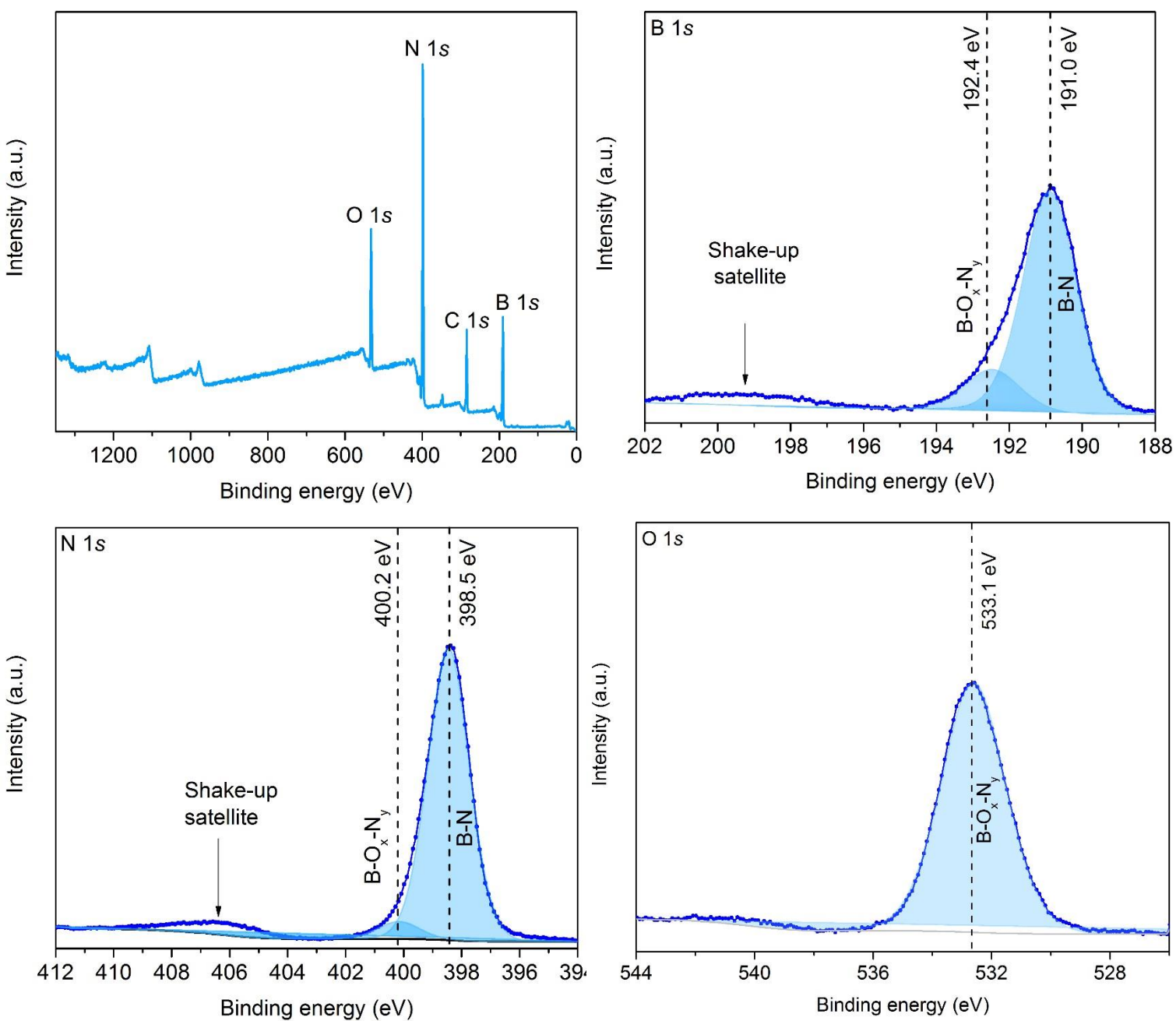


Figure S1. Survey spectrum and high resolution XPS core level spectra for B 1s, N 1s and O 1s with the key characteristic peaks and corresponding binding energies highlighted.

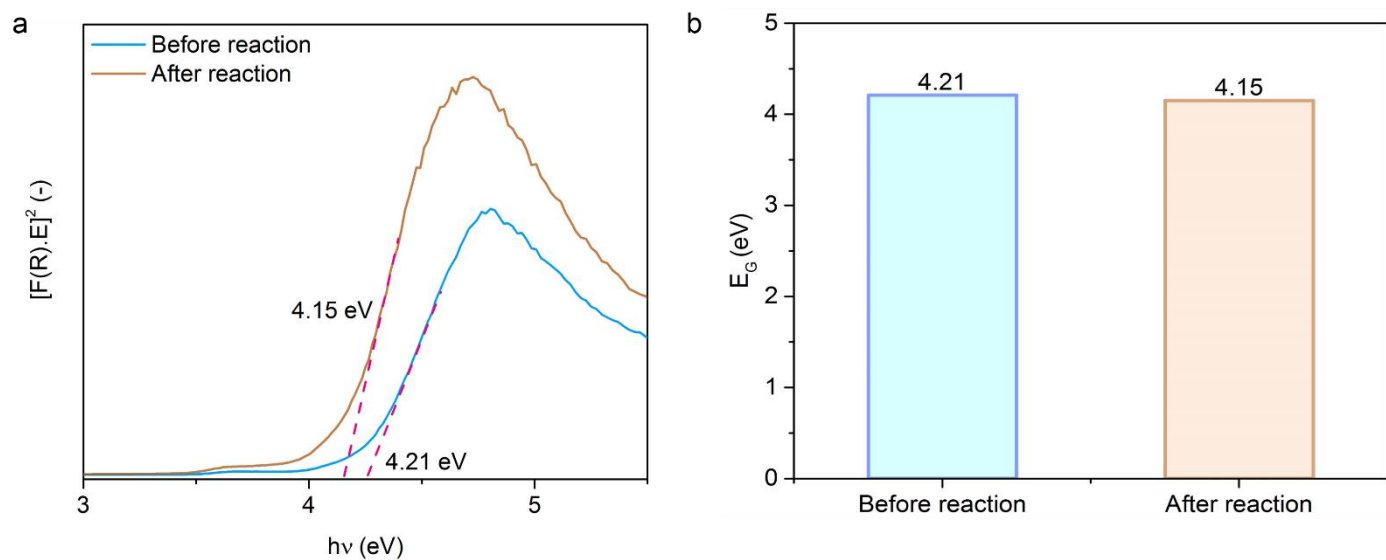


Figure S2 I (a) Tauc plot of the Kubelka-Munk function versus photon energy to determine the optical band gap of the porous BN material before and after photocatalytic CO₂ reduction reaction, (b) Optical band gaps of porous BN before and after the CO₂ photoreduction reaction.

Table S2. CO₂ adsorption capacities (25 °C) and specific CO evolution rates of the materials investigated in this study.

Sample	CO₂ adsorption capacity (mmol g⁻¹ STP)	CO evolution rate (UV-Vis) (μmol g⁻¹ h⁻¹)	CO evolution rate (Visible) (μmol g⁻¹ h⁻¹)
Porous BN	1.22	1.17	0.15
P25	0.21	1.08	n.d
g-C₃N₄	0.07	0.45	0.40
h-BN	0.03	0.01	n.d

n.d – none detected

Table S3. Summary of the CO evolution rates for porous BN for all of the photocatalytic CO₂ reduction reactions conducted.

Reaction	CO evolution rate (UV-Vis) ($\mu\text{mol g}^{-1} \text{h}^{-1}$)
UV-Vis (CO₂/H₂)	1.17
Visible (CO₂/H₂)	0.15
Blank run (no photocatalyst)	n.d
Dark run	n.d
N₂/H₂ run	n.d
¹³CO₂ isotopic test	1.10
<i>n.d – none detected</i>	

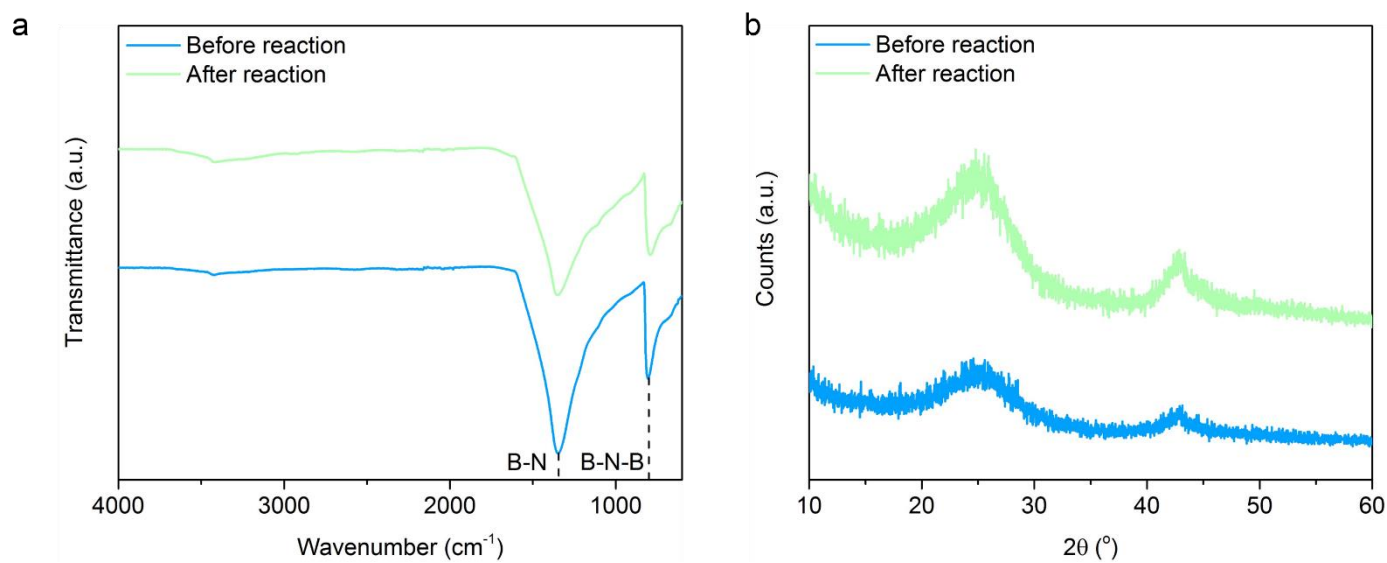


Figure S3. (a) Comparison of the FT-IR spectra of the porous BN before and after the CO_2 photoreduction reaction, with key characteristic bands highlighted, (b) Comparison of the XRD patterns of the porous BN before and after the CO_2 photoreduction reaction.

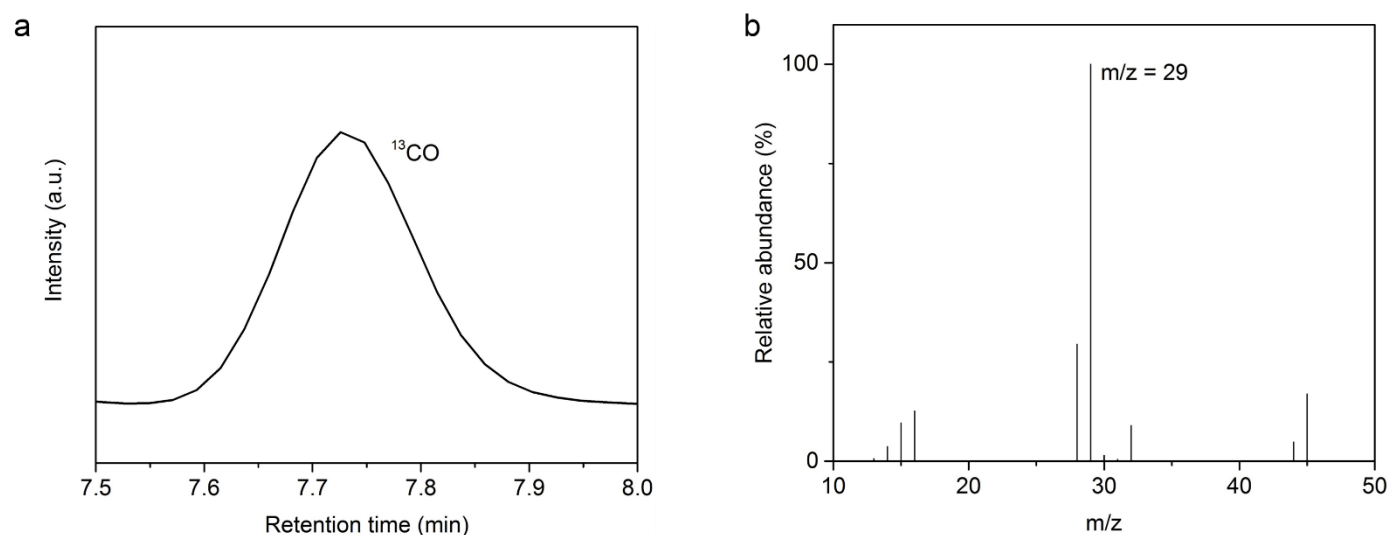


Figure S4. (a) Gas chromatogram illustrating the ^{13}CO peak observed with the photocatalytic $^{13}\text{CO}_2$ reduction system, (b) Mass spectra for the photocatalytic $^{13}\text{CO}_2$ reduction system with the peak corresponding to ^{13}CO ($m/z = 29$) indicated. All of the peak intensities have been scaled relative to the intensity of the $m/z = 29$ peak.

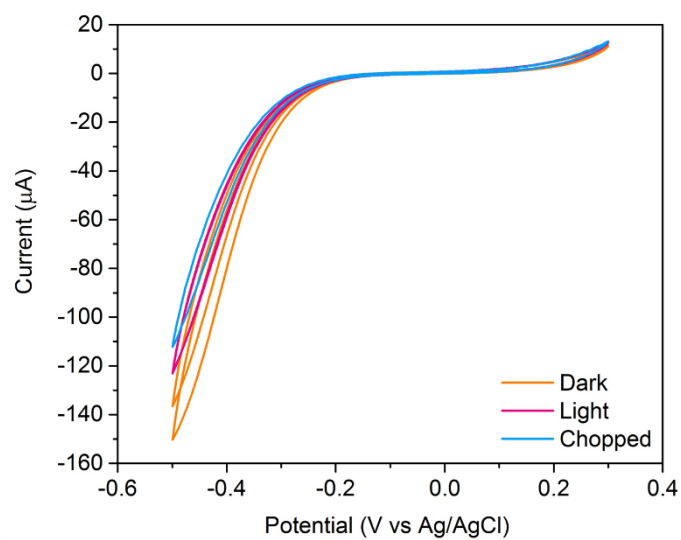


Figure S5. (a) Measured photocurrent response from cyclic voltammetry tests under dark, light, chopped (on/off) conditions.